Catalysis Science & Technology

Accepted Manuscript

This article can be cited before page numbers have been issued, to do this please use: N. Herrmann, A. Wolf, U. Schürmann, S. Mangelsen, C. Ruhmlieb, M. Behrens and J. Albert, *Catal. Sci. Technol.*, 2026, DOI: 10.1039/D6CY00548A.

ROYAL SOCIETY OF CHEMISTRY

rsc.li/catalysis

View Article Online
DOI: 10.1039/D6CY00548A

Dynamic CO_2 Methanation using coprecipitated Mg(Ni)O-supported Ni Catalysts

Nick Herrmann[a], Anna Wolf[b], Ulrich Schürmann[c], Sebastian Mangelsen[b], Charlotte Ruhmlieb[d], Malte Behrens[b], Jakob Albert[a]*

[a] Institute of Technical and Macromolecular Chemistry, Universität Hamburg, Bundesstraße 45, 20146 Hamburg, Germany

[b] Institute of Inorganic Chemistry, Solid State Chemistry and Catalysis, Kiel University, Max-Eyth-Straße 2, 24118 Kiel, Germany

[c] Department of Material Science, Synthesis and Real Structure, Kiel University, Kaiserstraße 2, 24143 Kiel, Germany

[d] Institute of Physical Chemistry, Universität Hamburg, Grindelallee 117, 20146 Hamburg, Germany

* E-Mail: jakob.albert@uni-hamburg.de

Abstract

The high demand for robust, cheap and efficient CO_2 methanation catalysts is constantly growing as the challenges are evolving and industrial relevance is increasing. In this work, a series of nanoscale nickel-magnesium oxide (NM) catalysts derived from a coprecipitated bimetallic single source precursor was compared to a commercial Ni/Al_2O_3 catalyst and an impregnated benchmark Ni/MgO catalyst. At 260 °C and 20 bar under steady-state conditions the best performing catalyst with a nominal molar nickel-to-magnesium ratio of 50:50 reached 92% CO_2 conversion with a CH_4 selectivity close to 100% under stochiometric conditions. This catalyst was then subjected to a range of temperatures, GHSVs and gas feed compositions for a 100 h time-on-stream resilience test showing no deactivation while effectively suppressing the competing RWGS reaction. The results suggest that coprecipitated NM catalysts are highly productive and stable surpassing industrial methanation Ni/Al_2O_3 catalysts in terms of activity, selectivity and GHSV endurance even under hydrogen deficient conditions.

Keywords: Dynamic CO_2 Methanation, Coprecipitation, Heterogeneous Catalysis, Dynamic operation

View Article Online
DOI: 10.1039/D6CY00548A

Introduction

The excessive emission of CO_2 into the atmosphere through human activities is one of the main contributors to climate change and its associated adverse effects. Reducing the emission and mitigating the effects of climate change is one of the biggest challenges of the 21st century. [1] Some large-scale industrial processes like refineries, cement and steel production are very hard to decarbonize directly. For those cases several technical solutions for carbon capture and storage (CCS) as well as utilization (CCU) processes have been proposed. [2–5]

On the one hand, CO_2 has potential as a C1 building block, but only a few industrial processes currently use CO_2 as a raw material. Existing applications include synthesizing urea [6,7], salicylic acid [8], and carbonates [9], but broader implementation of CO_2 utilization on an industrial scale has yet to be realized.

On the other hand, there are many proposed routes for integrating CO_2 as an energy vector and to prevent release in the first place. Such proposed routes involve the synthesis of methanol [10], dimethyl ether [11], Fischer-Tropsch products [12] and synthetic natural gas (SNG) [13]. However, most of these pathways remain challenging requiring further advances in catalysis and process engineering to improve efficiency, selectivity, and economic viability.

The methanation of CO_2 has emerged as a bridging technology for valorizing the captured CO_2 with green H_2 which is part of the 'Power-to-X' concept. This opens up the existing natural gas infrastructure as a long-term energy storage being both cost effective, lowering the overall capital expenditure for hydrogen storage and easily scalable. The Technology Readiness Level (TRL) is described to be around 7 on a scale of 1 to 9, with commercial systems already operating. [14–16]

The possible reactions generally involved in methanation include reduction of CO_2 and/or CO with hydrogen as shown in equations (1) and (2) both being highly exothermic. With CO_2 as a feedstock a prior endothermic reduction step via the reverse water-gas shift reaction (RWGS) (equation 3) can also take place:

$$CO_2 + 4\,H_2 \rightleftharpoons CH_4 + 2\,H_2O \qquad \Delta H_R = -165\ \text{kJ mol}^{-1} \qquad (1)$$

$$CO + 3\,H_2 \rightleftharpoons CH_4 + H_2O \qquad \Delta H_R = -206\ \text{kJ mol}^{-1} \qquad (2)$$

$$CO_2 + H_2 \rightleftharpoons CO + H_2O \qquad \Delta H_R = +41.0\ \text{kJ mol}^{-1} \qquad (3)$$

View Article Online
DOI: 10.1039/D6CY00548A

For the methanation reaction using Ni-based catalysts, multiple pathways are proposed but no consensus has been reached although it has been studied both theoretically and experimentally. [17,18] However, there is agreement that the support or promoter has a decisive influence. The "carboxyl pathway" can be observed in unsupported catalysts or compounds having an inert or acidic support material. The "formate route" is more profound in catalysts with a basic support (such as MgO) or with a strong metal support interaction (SMSI) [17,19]. Catalysts operating via the "carboxyl pathway" (*CO) split further into a route of direct C-O bond cleavage (*C) or a RWGS step with subsequential hydrogenation. The "formate pathway", on the other hand, does not involve the initial splitting off of oxygen, but rather the gradual addition of hydrogen to the *HCOO molecule and the subsequent formation of water. [17] For catalysts with a very high affinity for CO_2 adsorption, an associative mechanism has been observed, forming an active species (e.g., $*CO_3$) on the support. [20]

Regarding the engineering aspects of CO_2 methanation, recent work focusses on the dynamic behavior under fluctuating conditions, the shift in selectivity and the deactivation mechanisms. [21,22] A rack-type reactor involving a structured catalyst showed promising results without deactivation at 375 °C with high methane selectivity. [23] In general, when the feed of hydrogen falls below the stoichiometric ratio, the methanation reaction diminishes. Hot spots often lead to catalyst sintering which is accompanied by deactivation in most cases. [23,24] Thermodynamically, the methanation is also favored at lower temperatures but often lacks the energy to overcome the intrinsic energy barrier. In addition, lower reaction temperatures are favored by operational expenditure. [25]

Another challenge lies in managing the variability of green hydrogen production. Since hydrogen generation from renewable sources is inherently intermittent, fluctuations in gas composition and space velocity can significantly impact catalyst performance. [26] This shifts the window of opportunity for producing a constant stream of synthetic natural gas with high calorific value. Therefore, catalysts that are resilient to such drastic changes in operational conditions are highly desirable. [24]

This work investigates the performance of recently developed nanoscale nickel-magnesium oxide (Ni/Mg(Ni)O) catalysts (NM) derived from a coprecipitated bimetallic single source precursor [28] under fluctuating reaction conditions and their influence on the methanation activity in a fixed-bed

View Article Online
DOI: 10.1039/D6CY00548A

reactor. Different catalyst compositions in terms of nickel-to-magnesium ratios are tested and changes in the microstructure investigated. The objective is to determine beneficial reaction conditions, preferably at low temperatures allowing for high CO_2 conversion and high selectivity towards CH_4. Furthermore, the best performing catalyst is benchmarked to a commercial Ni/Al_2O_3 catalyst over a period of 100 h time-on-stream (TOS) to test the catalysts resilience and stability under dynamic reaction conditions simulating a potential realistic operating environment.

Experimental details

Materials & Catalyst Synthesis

Nickel nitrate hexahydrate (abcr, 99.9 %), magnesium nitrate hexahydrate (Merck, 99 %) and sodium carbonate anhydrate (Grüssing, 99.5 %) were used as starting materials for catalyst synthesis without further purification. The NM catalysts were synthesized by coprecipitating a 1 M $Ni(NO_3)/Mg(NO_3)$ solution in the targeted ratio with a 1.6 M Na_2CO_3 solution in an automated laboratory reactor system "OptiMax" by Mettler Toledo. A constant pH of 9 was controlled by dosing the precipitation agent simultaneously at a temperature of 5 °C. After an amount of 100 g of metal salt solution was dosed at a rate of 3.33 g/min, the slurry was immediately transferred into a PTFE lined steel autoclave, sealed and aged for 20 h at 100 °C. The product was afterwards washed via centrifugation with demineralized water until the conductivity of the centrifugate was below 100 µS/cm and dried overnight in air at 60 °C resulting in a bright green powder with a sum formula of $(Ni_{1-x}Mg_x)_{12}(CO_3)_8(OH)_6O \cdot y\,H_2O$ with x = 0.1, 0.3, 0.5. The calcination was then carried out for 3 h at 400 °C in glazed crucibles in a muffle furnace resulting in the black solid solution pre-catalyst $(Ni_{1-x}Mg_x)O$. Further details on the synthesis can be found in ref. [28]. The pre-catalysts $(Ni_{1-x}Mg_x)O$ could not be fully reduced to Ni/MgO, but some nickel remained oxidized in the support leading to a catalyst composition of $Ni/Mg_{1-y}Ni_yO$. For simplicity, the resulting support materials of the NM catalysts are summarized as Mg(Ni)O herein to highlight the fraction of unreduced nickel. The labeling of the samples follows the nominal relative Ni and Mg content and will be used in the following. A sample with a nominal ratio of metal cations of e.g. 90 % Ni to 10 % Mg is labelled NM9010.

17% Ni/Al_2O_3 was purchased from Riogen Inc. 10% Ni/MgO was prepared by wetness impregnation of MgO (Sigma Aldrich, 98%) with nickel nitrate hexahydrate (Subolab, 99%) in

View Article Online
DOI: 10.1039/D6CY00548A

water and subsequent removal at elevated temperatures, reduced pressures and calcination at 400 °C for 3 h. Nickel oxide was prepared by direct calcination of nickel nitrate hexahydrate at 400 °C for 3 h. The synthesis of Ni-In_2O_3/ZrO_2 has been described in literature before. [25] All catalyst materials were sieved to a size of 80-250 µm before being used in the fixed-bed reactor setup.

Catalyst Characterization

Inductively coupled plasma optical emission spectroscopy (ICP-OES) was used for determining the elementary composition of the synthesized catalysts. Hereby, 100 mg of a catalyst sample were digested in 5 mL of inverse aqua regia at 250 °C in a microwave oven filled up to 15 mL and being further diluted for the measurement. The sample was then atomized in an argon plasma and the composition was quantified using optical emission spectroscopy. The characterization was carried out on an ASCOR-spectrometer (Fa. Spectro).

Nitrogen physisorption was carried out with an Autosorb iQ-MP/XR analyzer (Fa. Quantachrome Instruments) at 77 K. First, the sample was degassed at 473 K at reduced pressure (10^{-1} mbar) for 10 h prior to analysis. Using the Brunauer-Emmett-Teller (BET) model, the specific surface area of the sample was determined and the pore volume was calculated by using the Barrett-Joyner-Halenda (BJH) model.

PXRD in transmission geometry was carried out on a Stadi P (STOE) diffractometer equipped with Mo-Kα_1 radiation (Johann-type Ge (111) monochromator) and a Mythen 1 K detector (Dectris). The samples were prepared as flat plates between two sheets of adhesive tape. For the PXRD measurements in reflection geometry a Panalytical Empyrean diffractometer equipped with Ni-filtered Cu Kα radiation and a PIXcel 1D detector was used.

Structure refinements were carried out using TOPAS Academic version 6.0. Instrumental line broadening was described using the fundamental parameter approach [26,27] as implemented in TOPAS and cross-checked against a measurement of LaB_6 (NIST SRM660c). Volume weighted domain sizes were calculated by the included routine as well. [28]

Transmission electron microscopy (TEM) was used to analyze the particle size, particle structure via electron diffraction as well as the element distribution via EDX elemental mapping. Samples were ground in butanol and then prepared on a TEM lacey-carbon Cu grid. Bright-field images and electron diffraction patterns were acquired using a Tecnai F30 G^2 (FEI) operating at 300 kV

View Article Online
DOI: 10.1039/D6CY00548A

acceleration voltage. The elemental maps were conducted on a probe Cs-corrected JEM-ARM200F NEOARM from JEOL (200 kV) equipped with two front and entry side positioned silicon drift EDX (100 mm2 area each) detectors.

Gas chromatography (GC) was carried out online using a Micro GC Fusion 2-Module system by Inficon. Both modules are feed with argon as a carrier gas and both have a thermal conductivity detector (TCD) for detection. Module A has a 10 m RT-Molsieve 5A column equipped with a backflush to detect the gases H_2, O_2, N_2, CH_4 and CO. Module B has a 12 m RT-Q-Bond column to detect the gases CO_2, CH_4, short chained alkanes and water.

Temperature-programmed desorption of CO_2 (CO_2-TPD) was measured using a ChemBET Pulsar (Fa. Quantachrome Instruments). A catalyst sieve fraction of 80-250 µm was used. Prior, the samples (0.05 g) were exposed to a N_2 gas flow (80 mL/min) and heated up to 200 °C (10 °C/min) for 1 h to remove surface H_2O, followed by cooling down to 40 °C. The sample was heated up again under H_2/N_2 (5/95 v/v) gas flow (80 mL/min, 10 °C/min) to 700 °C. The same sample was subsequently exposed to the CO_2 atmosphere at 40 °C. The sample was then heated up under a He gas flow (80 mL/min, 10 °C/min) to 700 °C and the desorbed CO_2 was measured via the TCD.

Reactor setup and catalytic evaluation

The methanation reactions were carried out in a stainless-steel (1.4571) fixed-bed reactor with an inner diameter of 4 mm and a maximum catalyst packing height of 80 mm. The thermocouple is pressed against the reactor wall in the middle of the packed bed. The reactor is surrounded by graphite composite material to ensure fast heat transfer and constant temperatures. A second reactor with the same dimensions is installed right next to the first reactor sharing the same gas supply. The gas flows were controlled by Bronkhorst El-Flow Select mass flow controllers and distributed via a heated 6 mm stainless-steel (1.4571) piping with a junction to distribute the gases to the reactors. Fine regulating valves and a Bronkhorst El-Flow Select mass flow meter at the outlet of reactor one were used to ensure even distribution of the gases to both reactors. The reactor outlets were connected to a 4-way Valco Sample valve to allow for easy switching of the gas sampling for the online GC. A schematic process flow diagram can be found in Figure S1. For setting up the reaction, usually 500 mg of catalyst (80-250 µm) were mixed with glass beads (250-300 µm), loaded into the reactor and fixed by glass wool plugs. Prior to the reaction, the catalyst was preformed. This includes a heating out at 400 °C for 60 min under nitrogen (100 $mL_N\ min^{-1}$) to

View Article Online
DOI: 10.1039/D6CY00548A

remove adsorbed water and gases, a reduction of the catalyst under a flow of hydrogen (25 $mL_N\ min^{-1}$) in nitrogen (75 $mL_N\ min^{-1}$) and a subsequent cooling to 200 °C under nitrogen. After the pretreatment the reactor pressure was raised to the desired level of 5-20 bar by adjusting the back-pressure regulators. The reactant gas stream had a stoichiometric ratio of CO_2/H_2 of 1/4 if not specified otherwise while being diluted in 80 vol% of nitrogen as a carrier gas to minimize the effect of gas volume shrinking during the reaction. The total feed gas flow rate was set to be 974 $mL_N\ min^{-1}$ resulting in a GHSV of 46.000 for each of both reactors. The temporal resolution of the micro GC sampling of the gas phase is set to 5 min. The mean residence time of the reactor was determined via displacement marking at a GHSV of 10.000 to be around 60 seconds. To determine steady state conditions, three consecutive gas samples were collected.

Calculations

The conversion X of CO_2 can be determined with the general equation (4). The number of moles n of CO_2 at the inlet can be estimated via the ideal gas law. The number of moles CO_2 after the reaction can be determined via the concentrations of CO_2 determined by the online GC of the product gas stream in equation (5). Because the methanation reaction is volume reducing, a correcting factor f_{cal} equivalent to the difference in nitrogen concentration is introduced to account for this.

$$X_{CO_2} = \frac{\dot{n}_{CO_2,in} - \dot{n}_{CO_2,out}}{\dot{n}_{CO_2,in}} \cdot 100 \quad (4)$$

$$\dot{n}_{CO_2,out} = \frac{\dot{n}_{CO_2,in} \cdot c_{CO_2,out} \cdot f_{cal}}{c_{CO_2,in}} \quad (5)$$

$$f_{cal} = \frac{c_{N_2,\,in}}{c_{N_2,\,out}} \quad (6)$$

The selectivity for methane and the CO side product if detected was calculated with equation (7). The catalyst productivity was calculated by equation (8) with respect to the amount of nickel derived from the elemental analysis.

$$S_{CH_4} = \frac{\dot{n}_{CH_4,out}}{\dot{n}_{CO_2,in} - \dot{n}_{CO_2,out}} \cdot \frac{|\nu_{CO_2}|}{\nu_{CH_4}} \cdot 100 \quad (7)$$

(8)

The gas hourly space velocity (GHSV) as a mean of relating the standard gas flow ($\dot{V}_N$) and the catalyst volume (V_{cat}) is calculated via equation (9).

View Article Online
DOI: 10.1039/D6CY00548A

$$\mathrm{GHSV} = \frac{\dot{V}_N}{V_{cat}} \tag{9}$$

The equilibrium conversions were calculated with Aspen Plus V12 using the property method of Peng-Robinson, minimizing Gibbs free energy (10).

$$p = \frac{RT}{V_m - b} - \frac{a\alpha}{V_m^2 + 2bV_m - b^2} \tag{10}$$

View Article Online
DOI: 10.1039/D6CY00548A

Results and Discussion

Aim of the following study was to further investigate the recently developed nanoscale nickel-magnesium oxide (Ni/Mg(Ni)O) catalysts (hereafter: NM) by Wolf et al. [29] regarding their catalytic performance in comparison to benchmark supported Ni catalysts both under fluctuating and dynamic conditions. At first, the NM catalysts with varying Ni content are compared to a commercial Ni/Al_2O_3 methanation catalyst as well as a wetness impregnated Ni/MgO and a $Ni-In_2O_3/ZrO_2$ catalyst at common methanation conditions. Next, the influence of temperature and pressure on the CO_2 conversion and selectivity of the NM catalyst will be discussed. Finally, the dynamic behavior of the NM5050 and the Ni/Al_2O_3 catalyst will be revealed and the structural changes of the NM5050 after 100 h TOS discussed.

I. Catalyst screening and characterization

In this section, the recently developed coprecipitated NM catalysts in different compositions are evaluated in comparison to the established Ni/Al_2O_3 as well as a classical Ni/MgO prepared by wetness impregnation and the neat support materials MgO and Al_2O_3, respectively. Based on previous results from literature [30] the catalysts were compared at 300 °C and 10 bar. Under these conditions, CH_4 selectivities above 90% and a CO_2 conversion of approximately 50% were expected. The composition of the feed gas was a stoichiometric CO_2/H_2 1:4 mixture. To minimize the effect of the reduced volume during feed conversion, 80% of nitrogen was used as a diluent gas. The results of the methanation under steady-state conditions reached after 15 min TOS are shown in Figure 1.

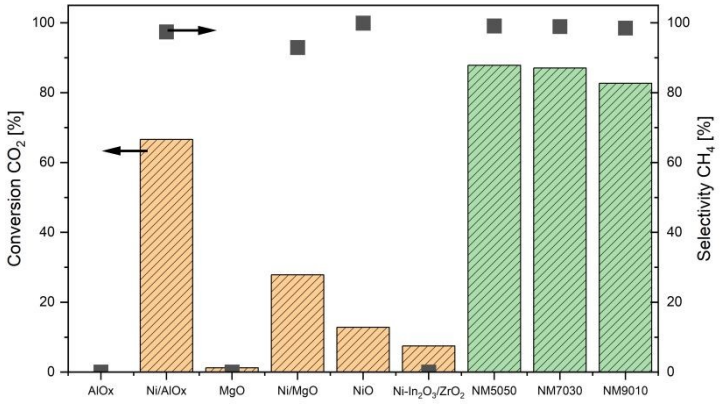

Figure 1: Catalyst screening for methanation under steady-state conditions. Reaction conditions: T = 300°C, p = 10 bar, m_{cat} = 0.5 g, $CO_2/H_2/N_2$= 4:16:80, GHSV = 50 000 h^{-1}.

View Article Online
DOI: 10.1039/D6CY00548A

The commercial Ni/Al_2O_3 catalyst showed a CO_2 conversion of 66% with a high methane selectivity of 97% under the applied reaction conditions. The neat Al_2O_3 support material did not show any methanation activity by itself. This also applies to the MgO support material. The Ni/MgO catalyst showed both a lower CO_2 conversion of only 29% as well as a slightly lower methane selectivity of 94%. Comparing this to a Ni-MgO catalyst prepared by sol-gel synthesis under similar reaction conditions, a CO_2 conversion of up to 95% at 300 °C can be achieved, implying the importance of tuning catalyst synthesis conditions. [31] In contrast, neat NiO, which is obtained by direct calcination of nickel nitrate, exhibits a very high methane selectivity of 99.9%, but at fairly low CO_2 conversion of only 13%. Moreover, the $Ni\text{-}In_2O_3/ZrO_2$ catalyst also showed no methanation activity at all. The influences of the support material and the preparation method on the methanation activity of Ni-based catalysts have been widely studied elsewhere. [32–37] By optimizing the microstructure and metal support interaction the effects are mitigated.

The NM catalysts derived from a coprecipitated precursor showed remarkably high activity for CO_2 methanation. Methane selectivity was found to be above 98%, and CO_2 conversion was above 80%, for all tested compositions. The conversion and selectivity were highest for the NM5050 catalyst with the lowest amount of Ni (Table 1). With increasingly more Ni in the NM catalyst, the overall activity decreased.

Table 1: Elemental analysis and textural properties of the nickel-based catalysts applied in this study.

Catalyst	**Nickel content[a] / wt%**	**Surface area[b] / m^2g^{-1}**	**Pore volume[c] / cm^3g^{-1}**	**Mean pore radius[c] / nm**
Ni/Al_2O_3	17.0	151	0.383	4.05
Ni/MgO	10.0	7.8	0.038	3.17
$Ni\text{-}In_2O_3/ZrO_2$	0.76	81	0.216	3.70
NM5050 - fresh	48.2	288	0.232	1.48
NM7030 - fresh	58.1	122	0.161	2.52
NM9010 - fresh	62.9	129	0.065	1.57

[a] Determined by ICP-OES, [b] BET surface area determined by N_2 physisorption of unreduced material, [c] Determined by BJH-Method from the adsorption isotherm.

In the next step, a closer investigation of potential changes of the NM catalysts in specific surface area and chemical composition of the starting material (labelled "fresh") was carried out. These calcined materials consisting of solid solution oxides of varying compositions ($Ni_{1-x}Mg_xO$) [29] are compared to preformed materials (i.e. those that have undergone pre-treatment) and spent samples after passivation. The passivation of the catalyst surface was done after the reactor had

View Article Online
DOI: 10.1039/D6CY00548A

cooled down to room temperature whereby the catalyst bed was exposed to air for roughly 15 h by opening the reactors top screw slightly to allow for the intrusion of air, passivating the material. These were then further subjected to analysis (Table 2).

Table 2: Comparing the elemental composition and surface area of the untreated NM catalysts with the preformed and post-reaction NM catalysts after passivation.

Catalyst		**Ni content[a] /atom%**	**Mg content[a] /atom%**	**Surface area[b] /m^2g^{-1}**
NM5050	Preformed	63.9	36.1	160
	Post-reaction	64.3	35.7	77
NM7030	Preformed	76.1	23.9	87
	Post-reaction	75.9	24.1	56
NM9010	Preformed	91.2	8.8	13
	Post-reaction	90.9	9.1	9.6

[a] Determined by ICP-OES, [b] BET surface area determined by N_2 physisorption.

By analyzing the elemental composition of the NM catalysts, no leaching of Ni was observed as the relative atomic ratio of Ni to Mg remained constant as expected, both for the preformed and post-reaction samples. Regarding the catalyst surface area, it was observed that the surface area and pore volume of the NM catalysts were roughly halved during the preforming step at 400 °C in a hydrogen atmosphere for NM5050 and NM7030. This suggests that the segregation of metallic nickel out of the solid solution during the reduction results in strong changes in the catalyst's microstructure and porosity. This effect was most pronounced for the nickel-richest NM9010 catalyst resulting in only a tenth of the original surface area of only 13 m^2g^{-1}. Despite the decrease of surface area during the preforming, the activity for all the NM coprecipitated catalysts was observed to be much higher than for the Ni/Al_2O_3 and the impregnated Ni/MgO catalyst. The total amount of nickel does not seem to have the main influence on the CO_2 conversion and CH_4 selectivity under the performed reaction conditions but rather the unique microstructure of the NM catalysts resulted in increased CO_2 conversion. [28] Comparing the catalysts after the preforming with the catalysts post reaction, the surface area decreased even further by ~ 50 % for NM 5050 and ~ 30 % for NM7030 and NM9010, respectively.

To elucidate the changes further, powder XRD (PXRD, Figure S8) and HR-TEM measurements (Figure S8) of the NM catalysts were performed. At first, the presence of a solid solution of the starting material $Ni_{1-x}Mg_xO$ was confirmed by Rietveld refinement in all three cases (Figure S3). The three calcined samples differed in terms of the cell parameter a of their cubic rock-salt-type structure due to their differences in composition. Whilst the NM5050 has a lattice parameter a =

View Article Online
DOI: 10.1039/D6CY00548A

4.2057(8) Å, the lattice parameter of NM7030 is a = 4.1889(3) Å and for NM9010 a = 4.1814(3) Å. With increasing Ni content, the cell parameter a decreases to resemble the cell parameter of pure NiO (NiO [38] a = 4.17610(4) Å, MgO [39] a = 4.217(1) Å). The domain sizes are similar and range from 2.70(6) nm for NM5050 to 4.75(7) nm and 4.45(6) nm for NM7030 and NM9010.

During the preforming step, the nickel starts to partially segregate and forms metallic domains (Figure 2). This effect is quite pronounced in the NM9010 catalyst with the highest nickel content. Most of the Ni is present in the metallic form as evidenced by intense reflections. The domain size was determined to be 37(2) nm. In the diffraction pattern of NM9010 additional minor reflections are assigned to elemental silicon, which was not observed in any other samples and is treated as a neglectable contamination. The NM7030 had less metallic nickel segregated from the solid solution after preforming, resulting in smaller crystallite sizes of 6.6(7) nm. The NM5050 catalyst showed almost no changes in the PXRD compared to the calcined state. No metallic nickel could be determined via Rietveld refinement after reduction and passivation although the catalytic results strongly suggest the presence of metallic nickel in the working catalyst. Likely, the metallic nickel domains were small and reactive enough that they completely re-oxidized during passivation. However, by adding a phase of pure NiO to the refinement (in case it had been segregated and then fully re-oxidized) no significant improvement of the fit was reached (Figure S4). It is assumed that the domains of the NiO are too small and add only to the background. The remaining solid solution oxide has a larger domain size of 3.97(6) nm to 4.4(2) nm suggesting only slight sintering of the support. All difference plots can be can be found in the supporting information (Figures S3-S6). Altogether and in accordance with literature reports, the resulting nickel metal crystallize size of the NM catalysts depends less on the crystallize size of the fresh catalyst, but more strongly on the composition, which determines the reducibility. TPR investigations [29,40] have shown that Mg-rich solid solution oxides are harder to reduce, but yield smaller nickel metal crystallites, in accordance with the results reported here.

View Article Online
DOI: 10.1039/D6CY00548A

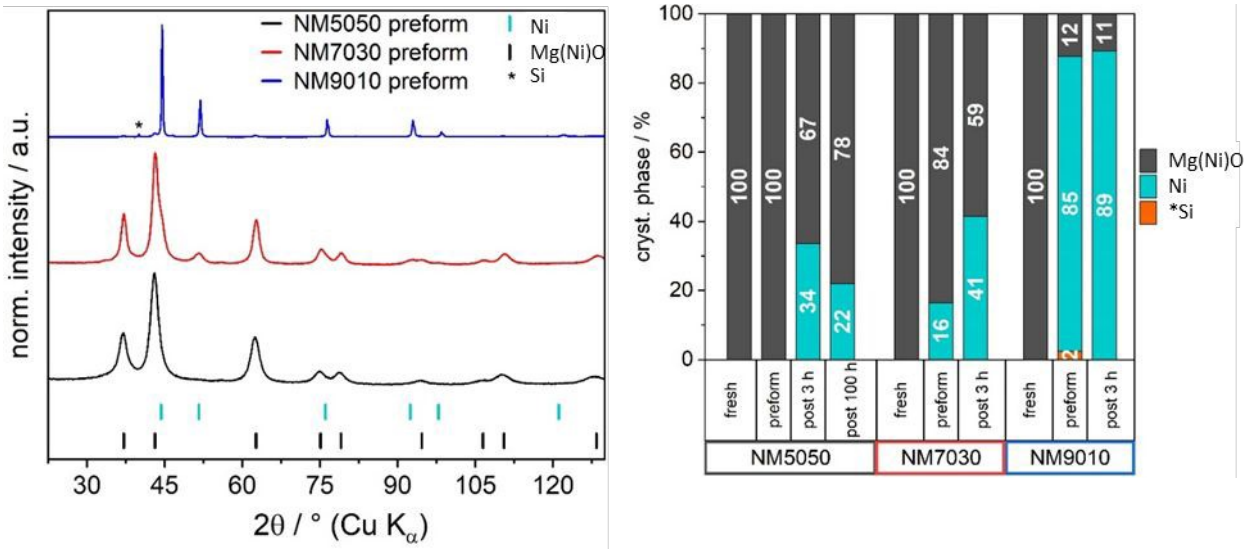

Figure 2: Powder XRD patterns for the preformed and passivated catalysts of various composition. The small additional reflections in the sample of NM9010 originate from a silicon phase marked with an asterisk (left). Quantification of crystalline phases for the different stages of the catalysts after passivation, derived from the Rietveld refinements (right). The label Mg(Ni)O stands for the support phase, an after preforming nickel-depleted oxide solid solution ($Ni_{1-x}Mg_x$)O with variable Ni content.

After the catalyst screening and the samples being 3 h TOS, further changes in phase composition and crystallite size could be revealed. Regarding the NM5050 catalyst, the post reaction sample shows clear reflections for metallic Ni with a domain size of 5.6(3) nm even after passivation suggesting crystallite growth and/or increase in the degree completion of reduction during the initial reaction phase. The previously observed general dependency on composition and reducibility is also maintained for the other NM catalysts as the phase fraction of metallic Ni for the NM7030 is larger and largest for NM9010. The Ni domains of NM9010 stayed constant in size (37(2) nm), suggesting that it reached a stable form after the preforming. The NM5050 and NM7030 are still changing in the methanation atmosphere. The crystallite size of nickel for the NM7030 increased from 6.6(7) nm to 11(2) nm. The larger fraction of MgO in the catalyst seems to protect the particles from sintering.

In all cases the remaining oxide is not pure MgO, but a Ni depleted $Ni_{1-x}Mg_xO$ denoted Mg(Ni)O since Ni is not fully reduced. The remaining fraction of Ni in the solid solution varies by stage and catalyst composition, ranging from roughly 30% up to 66% (Table S1). However, the presence of pure NiO (originating from metallic Ni after passivation) cannot be excluded, lowering the amount of Ni in the solid solution. Nevertheless, the total ratio of Ni to Mg atoms derived from the PXRD refinements is stable and matches the reported ICP-OES values (Table 2) within a reasonable margin. Moreover, a high nickel dispersion and uniform nickel and magnesium distribution can be

View Article Online
DOI: 10.1039/D6CY00548A

seen for all NM catalysts by TEM-EDX elemental mapping (Figure S9) except NM9010 where Ni agglomeration has been observed in accordance with previously reported results [29] and with the results gained by PXRD.

II. Effect of temperature on CO_2 conversion at steady-state conditions

The next step was to find out at what temperatures each of the NM catalysts performs best. All NM catalysts were heated from 200 to 400 °C in 20 °C steps and the outlet gas compositions measured three times to ensure the system being in steady-state conditions after 15 min. The results are shown in Figure 3.

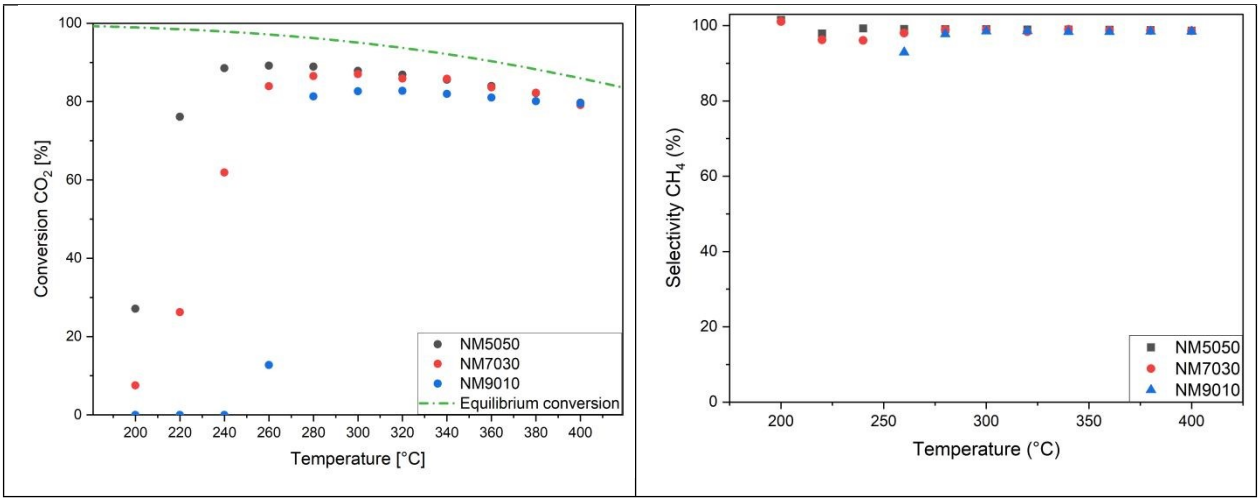

Figure 3: Conversion (left) and selectivity (right) for NM catalysts of various compositions. Reaction conditions: T = 200-400°C, p = 10 bar, m_{cat} = 0.5 g, $CO_2/H_2/N_2$= 4:16:80, GHSV = 50 000 h^{-1}.

By comparing the CO_2 conversion of the different NM catalysts, it is apparent, that the NM5050 catalyst is the most active, already exhibiting 76% conversion at 220 °C. The maximum conversion of 89% was found to be at 260 °C. With a further increase in the reaction temperature, the conversion is reduced, since the thermodynamic equilibrium has almost been reached. The NM7030 catalyst is also active at temperatures below 260 °C but does not reach the same level of activity as the NM5050 catalyst. It reaches highest conversion of 87% at 300 °C. At higher temperatures, the activity does align with the NM5050 catalyst. Differently, the NM9010 catalyst showed the lowest performance. It shows no measurable CO_2 conversion up to 260 °C whereby the highest conversion is reached at 320 °C with 83%. The methane selectivity for all three catalyst was around 98% at each observed temperature. Furthermore, none of the catalyst showed any signs

View Article Online
DOI: 10.1039/D6CY00548A

of deactivation. This was ensured by setting the screening conditions (Figure 1) after the temperature variation, for which the same conversions were obtained.

These results demonstrate the significant influence of the catalyst composition on low-temperature activity, while maintaining consistently high methane selectivity across all samples. The remarkable performance of NM5050 suggests this composition provides the most favorable balance between active site availability and catalytic functionality. This enables high CO_2 conversion at relatively low temperatures. In contrast, NM7030 and NM9010 require higher temperatures to achieve comparable conversions, indicating slower reaction kinetics under mild conditions.

It became apparent, that the amount of Ni and Mg has a significant influence on the methanation activity. To further investigate whether substrate adsorption plays a role, CO_2 TPD experiments were carried out to reveal possible differences between NM catalysts with different Ni content (Figure 4).

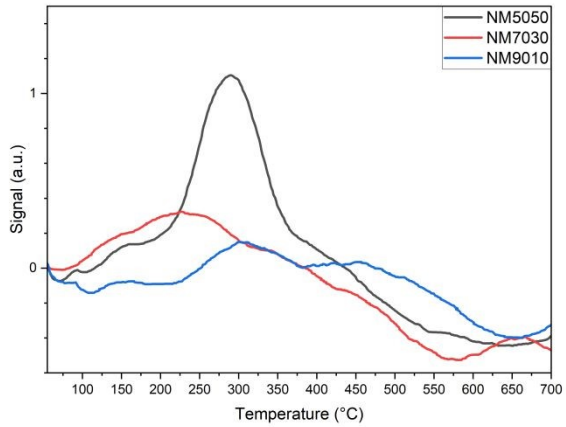

Figure 4: Comparing the NM catalysts with CO_2 TPD after reduction.

After the NM catalysts have been reduced with 5% H_2 in N_2 at 700 °C, the catalysts were exposed to CO_2 at 40 °C, followed by nitrogen and the TPD heating to determine the amount and strength of acid sites that bind the CO_2 from the reaction gas. The NM5050 catalyst showed a distinct desorption peak at 300 °C, which is attributed to moderately strong bound CO_2. The significantly higher peak integral of the NM5050 indicates substantially greater CO_2 uptake on its surface compared to the other NM catalyst. Notably, the integrated area is three times as higher than for the NM9010 (Table S2). A lot more CO_2 was bound to the catalyst surface compared to the other NM catalyst, explaining its high activity. The NM7030 has less and rather loosely bound CO_2,

View Article Online
DOI: 10.1039/D6CY00548A

being desorbed at 200 °C. For the NM9010 catalyst it does not seem like that any of the introduced CO_2 was able to be reversely bound. Compared to neat MgO, making up most of the catalyst, various active sites at temperatures below 100 °C have been found before. [41] This could indicate, that the CO_2 has been bound rather loosely and immediately desorbed after switching to nitrogen. This trend of lower desorption temperatures can be explained with the high basicity of MgO and its varying content in the three NM catalysts.

III. Effect of reaction pressure at steady-state conditions

Building on the previous analysis of the effects temperature exerts on the NM catalysts at a fixed pressure of 10 bar, the next step was to evaluate the influence of reaction pressure on catalyst performance at steady-state conditions. Experiments were conducted at 5 ,10 and 20 bar to evaluate the effects on CO_2 conversion and overall methanation efficiency. As before, the system quickly reached a steady-state after 15 min, confirmed by three identical consecutive measurements of the gas phase composition. This approach enabled a direct comparison of the catalysts behavior under different pressure conditions (Figure 5).

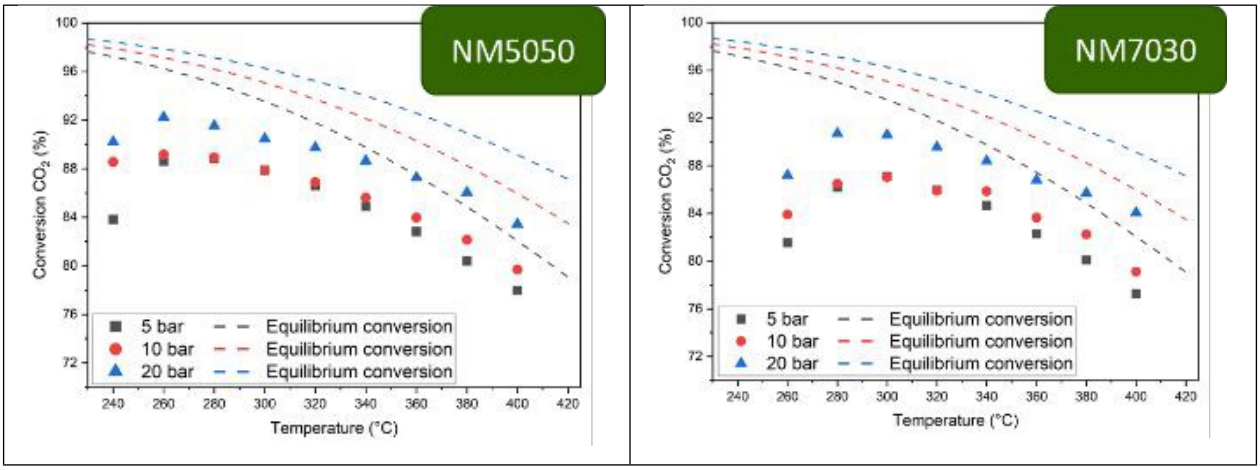

View Article Online
DOI: 10.1039/D6CY00548A

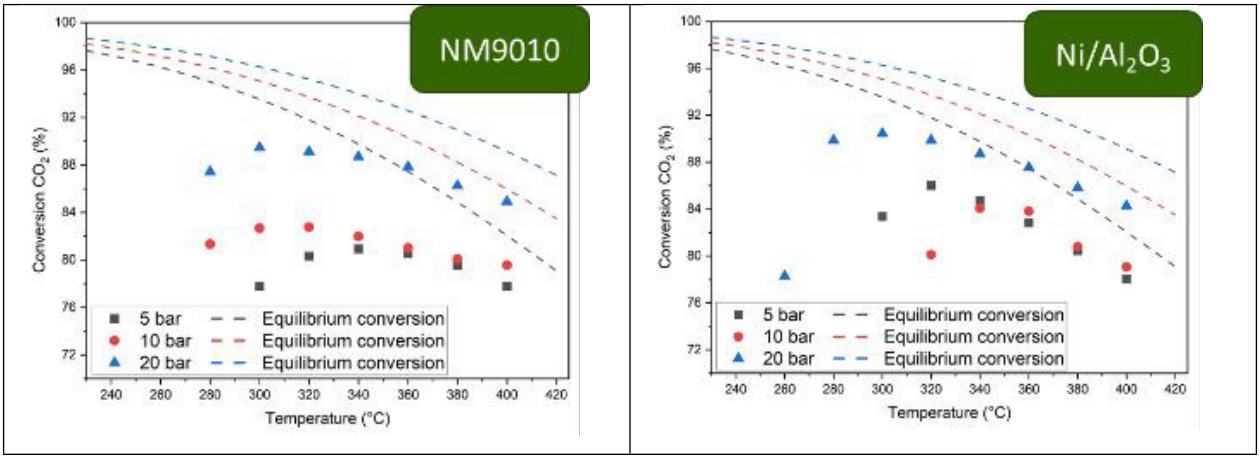

Figure 5: Performance comparison of different catalysts regarding the influence of different reaction pressures on CO_2 conversion. Displaying only the high conversion range above 70%. Reaction conditions: T = 200-400°C, p = 5-20 bar, m_{cat} = 0.5 g, $CO_2/H_2/N_2$= 4:16:80, GHSV = 50 000 h^{-1}.

In general, the increase in CO_2 conversion from 5 to 10 bar is miniscule. Increasing the reaction pressure further from 10 to 20 bar also has only a negligible effect with a 3% higher CO_2 conversion to methane using the NM5050 catalyst at 260 °C. The same holds true for the NM7030 catalyst with slight deviations and the shift towards higher temperatures with the highest conversion at 20 bar and 280 °C. The NM9010 catalyst exhibited the highest conversion only above 280 °C. It also has the highest increase in conversion with up to 89% at 300 °C and 20 bar compared to just 82% at 10 bar. Compared to the Ni/Al_2O_3 catalyst with only 20wt% Ni loading the NM9010 catalyst showed the same activity at 20 bar, despite the higher Ni loading, which might be due to the higher surface area of the Ni/Al_2O_3 catalyst. Interestingly, for all of the investigated catalysts, the activities started to merge for 5 and 10 bar. This trend was thermodynamically calculated before and matches our experimental findings. [42] The methane selectivity was usually at 98% for all catalysts at each pressure, besides some deviations at lower CO_2 conversion for the less active NM9010 and Ni/Al_2O_3 catalyst (Figure S7).

Regarding that hydrogen generation via water electrolysis can be performed at elevated pressures, it could be favorable for the methanation to take place at elevated pressures as well, feeding the methane directly into the gas grid. Park et al proposed that the levelized cost of synthetic natural gas is lowest at 11 bar showing the potential of increased pressure in methanation. [43] In addition, Lv et al. describe that methanation can be viable at 1 bar as well as 30 bar but the recovery of waste heat is most important to be competitive. [44] Further techno economic analysis would be needed to determine if the increased reaction pressure could yield synthetic natural gas more cost effective then at low reaction pressure with reduced yields but with more refining stages.

View Article Online
DOI: 10.1039/D6CY00548A

IV. 100 h Resilience Test: comparing the NM5050 with a commercial Ni/Al_2O_3 catalyst

In the data shown above, the NM5050 catalyst was found to be the most active methanation catalyst under methanation conditions of 260 °C and 20 bar. To investigate the resilience of the NM5050 catalyst in comparison to the commercial Ni/Al_2O_3 catalyst, the reaction conditions were varied over 100 h time-on-stream, whereby both catalysts were compared directly by loading the same catalyst mass into the reactor. The objective is to determine if and under what conditions the catalyst loses its activity, and whether this loss is reversible by returning to steady state conditions. Regarding possible fluctuations in the gas feed, lowering the H_2 to CO_2 ratio, reduced gas flow, increasing contact times and changes in temperature should simulate away from the steady state. The test is designed to return to steady-state conditions with the highest activity after increasingly harsher conditions. In the first step, the reaction conditions were fixed for the first 24 h at the point of highest CO_2 conversion (260 °C, 20 bar) for the NM5050 catalyst (Figure 6).

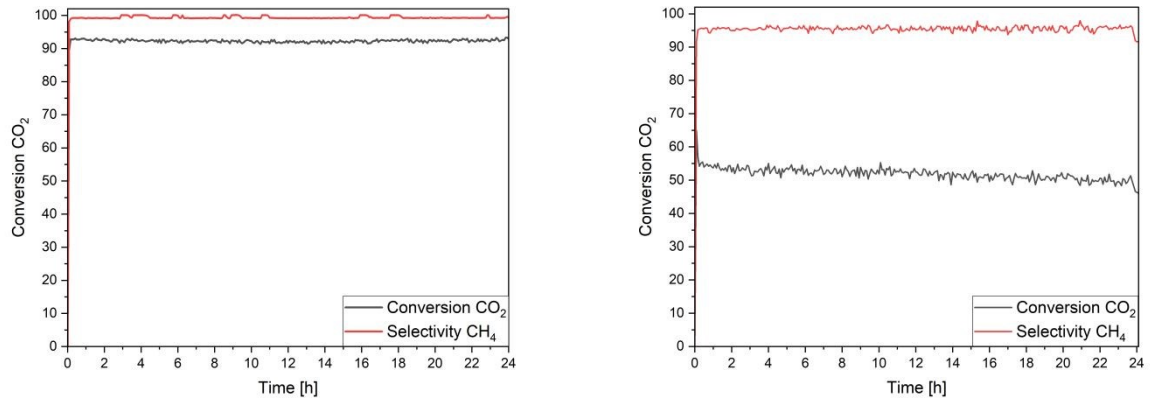

Figure 6: First 24 h of the resilience test, NM5050 (left) and Ni/Al_2O_3 (right). Reaction conditions: T = 260°C, p = 20 bar, m_{cat} = 0.5 g, $CO_2/H_2/N_2$= 4:16:80, GHSV = 50 000 h^{-1}.

The NM5050 catalyst did not show any signs of deactivation during the first 24 h. The CO_2 conversion throughout was at around 92% with a methane selectivity of around 99%. The Ni/Al_2O_3 catalyst in comparison started at a much lower conversion of 55% and decreased steadily to 50% during 24 h time-on-stream. The selectivity did not change but was slightly lower with 95% with the remaining 5% being CO from the competing RWGS reaction. During the following 24 h of reaction, the dynamic behavior of the catalyst was investigated by changing the gas phase composition. The stoichiometric ratio CO_2/H_2 of 1/4 was reduced for a period of three hours to 1/3. Afterwards, the stoichiometric gas phase composition was reapplied for a period of two hours. The

View Article Online
DOI: 10.1039/D6CY00548A

same procedure was then employed to test the catalyst response on a gas phase composition of 1/2 and 1/1, respectively (Figure 7).

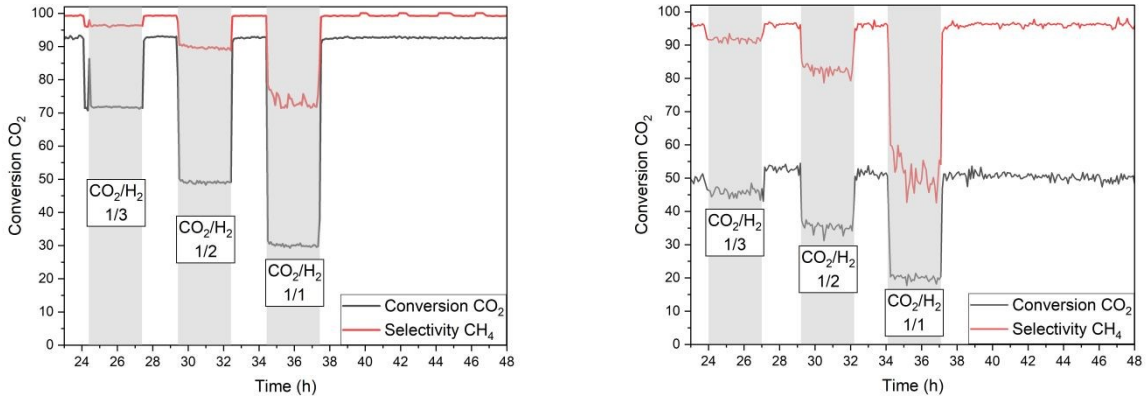

Figure 7: Second 24 h of the resilience test and variation of CO_2/H_2, NM5050 (left) and Ni/Al_2O_3 (right). Reaction conditions: T = 260°C, p = 20 bar, m_{cat} = 0.5 g, $CO_2/H_2/N_2$= 4:4-16:80-92, GHSV = 50 000 h^{-1}.

As expected, the CO_2 conversion dropped significantly with a sub-stoichiometric ratio for both catalysts. Even though the drop in activity is more pronounced for the NM5050 catalyst in relative values due to the higher overall CO_2 conversion, its performance is still superior in absolute values. The selectivity is not as strongly affected. In between, when the stoichiometric composition was reinstated, the activity of the NM5050 catalyst was reverted back immediately to the initial activity during the first 24 h. There is no sign of deactivation. Even after being exposed to a preferred atmosphere for RWGS reaction with a CO_2/H_2 ratio of 1/1, the selectivity was still above 70% although the CO_2 conversion dropped to about 30%.

The performance of the Ni/Al_2O_3 catalyst is similar, with lower overall conversion and selectivity. Interestingly, after the first step at 27 h on stream the Ni/Al_2O_3 catalyst has recovered some of its activity and showed a CO_2 conversion of 53%. However, this activity cannot be retained over the following hours of the resilience test. In conclusion, the NM5050 catalyst is more effective than the Ni/Al_2O_3 catalyst at suppressing the RWGS reaction when the gas composition is varied towards H_2 deficiency. Notably, the NM5050 catalyst performs similar at a CO_2/H_2 ratio of 1/2 as the Ni/Al_2O_3 catalyst does after 24 h time on stream with a ratio of 1/4.

The following variation of the GHSV after 48 h on stream investigated the influence of residence time during the methanation reaction on the catalyst activity. For this case, the GHSV was reduced from 50 000 h^{-1} to 3 000 h^{-1}. This was done in four one-hour stages, each with a halved gas flow rate, until the initial conditions were set again (Figure 8, magnified).

View Article Online
DOI: 10.1039/D6CY00548A

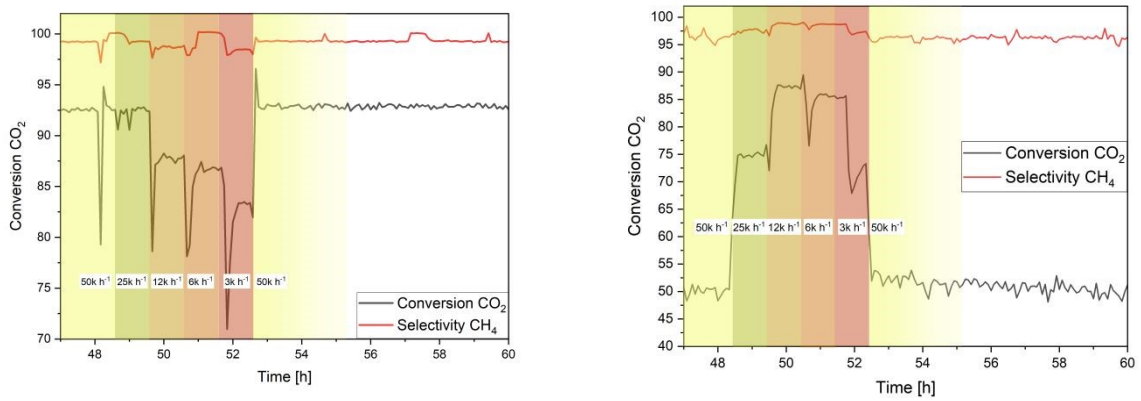

Figure 8: Influence of GHSV variation on the catalyst activity after 48 h time on stream, NM5050 (left) and Ni/Al_2O_3 (right). Reaction conditions: T = 260°C, p = 20 bar, m_{Kat} = 0.5 g, $CO_2/H_2/N_2$= 4:16:80, GHSV = 50 000-3 000 h^{-1}.

The methane selectivity does not seem to be significantly affected by the GHSV in this regime, remaining nearly constant throughout the variation for both catalysts. Regarding the CO_2 conversion of the NM5050 catalyst a simple correlation can be observed. With lower space velocities and therefore longer residence times the conversion is slightly lower during each of the four stages. Yet reducing the GHSV from 50 000 to 25 000 h^{-1} showed no significant difference in conversion, indicating that a maximum might have been reached. Higher space velocities appear to favor the performance of the NM5050 catalyst and could enhance absolute CO_2 conversion within a shorter timeframe. [29] The Ni/Al_2O_3 catalyst on the other hand seems to have an optimal space velocity of 12 000 h^{-1} with the highest CO_2 conversion of 87% matching the NM5050 catalyst at this stage. By reducing the space velocity further, the conversion decreases again being below that of the NM5050 catalyst. Nonetheless, after increasing the gas flow back to a space velocity of 50 000 h^{-1}, both catalysts immediately regained their prior activity. By looking at the overall conversion of CO_2 per unit of time, the NM5050 catalyst shows significantly higher activity than the Ni/Al_2O_3 catalyst at low temperatures of 260 °C and high space velocities. It could be assumed, that by lowering the GHSV and in turn lowering the overall gas flow, the effect of cooling is less pronounced. This results in a higher exit temperature, reducing the equilibrium yield. By comparing both NM5050 and Ni/Al_2O_3, the conversion is reduced for both systems below a GHSV of 6 000 h^{-1}. This suggests that above this GHSV, the addition of colder purge gas is enough to lower the reaction temperature.

In the final stage of the resilience test, both catalysts were exposed to higher reaction temperatures of up to 400 °C to figure out if this will lead to any form of catalyst deactivation (Figure 9).

View Article Online
DOI: 10.1039/D6CY00548A

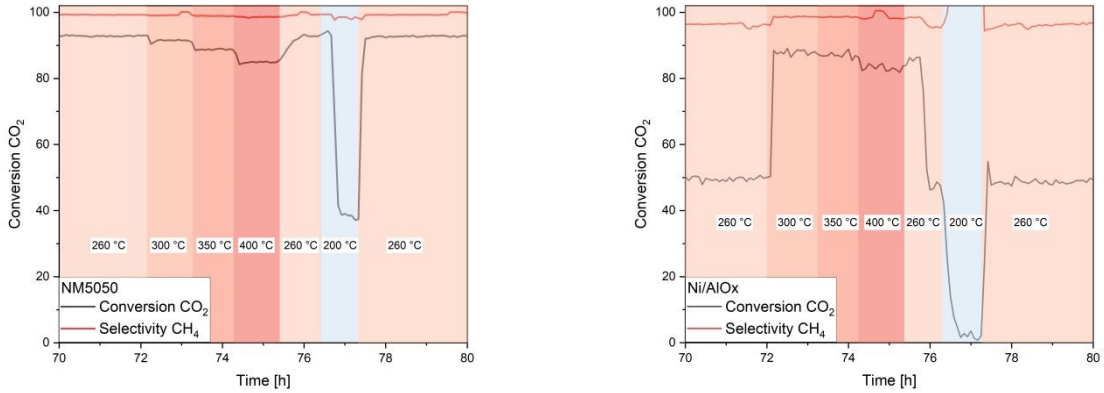

Figure 9: Influence temperature variation on the catalyst activity after 72 h time on stream, NM5050 (left) and Ni/Al_2O_3 (right). Reaction conditions: T = 200-400°C, p = 20 bar, m_{cat} = 0.5 g, $CO_2/H_2/N_2$= 4:16:80, GHSV = 50 000 h^{-1}.

In agreement with the results from the previous experiments, the CO_2 conversion using the NM5050 catalyst is slightly reduced at higher temperatures whilst the selectivity is unaffected. The activity was regained after cooling back down to 260 °C, steadily increasing the conversion during that phase. Even after the catalyst has been cooled down to 200 °C and being heated up again to 260 °C, the activity remains the same until the final hour of the 100 h resilience test. The Ni/Al_2O_3 catalyst does show an increased CO_2 conversion with higher temperatures. At 200 °C only marginal amounts of methane could be detected most likely being some residue gas. The Ni/Al_2O_3 catalyst has retained its activity of around 50% CO_2 conversion during the last 24 h on stream.

V. Characterization of the NM5050 catalyst after the 100 h resilience test

After the resilience test, which represents not only 100 h TOS but also includes the variation of the gas phase composition and more importantly a significant increase in temperature, remarkably the crystallite size of the Ni domains increased only by less than one nanometer from 5.6(3) nm to 6.4(7) nm. These findings, combined with immutable conversion and selectivity, suggest and substantiate the creation of a stable, highly productive catalyst. Comparing the powder XRD patterns of the NM5050 catalyst after 3 h under steady-state conditions with the ones after the 100 h resilience test, slight changes can be observed (Figure 10).

View Article Online
DOI: 10.1039/D6CY00548A

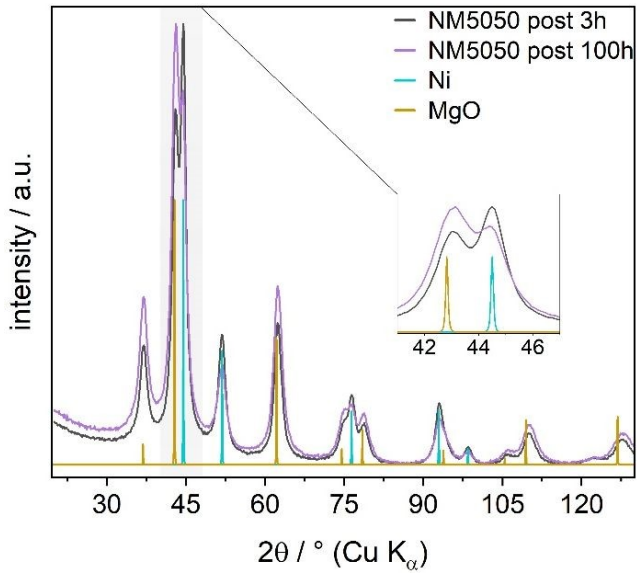

Figure 10: Comparison of powder XRD patterns of the NM5050 catalyst after 3 h and 100 h TOS (resilience tests) alongside calculated patterns of the constituting phases for MgO [39] and Ni [45].

Over the course of 100 TOS the intensities for metallic Ni and the solid solution oxide show opposite trends. The phase quantification shows an increase in the oxidic component and a decrease of metallic Ni accordingly (Figure 2). After the resilience test of the NM5050 the passivated post-reaction catalyst retains 22% metallic Ni, which was 34% after the catalytic testing for 3h. Since the testing program subjects the catalyst to a large variety of different conditions, the effect of each influencing factor cannot be assigned individually. However, a significant decline in conversion and selectivity could not be observed, suggesting that the cause for the changes in phase composition might be an effect of the passivation.

EELS measurements of the spent NM5050 catalyst (Figure S11) showed signals at 852 eV and 869 eV corresponding to the Ni-L_3 ($2p_{3/2}\rightarrow$ 3d) and Ni-L_2 ($2p_{1/2}\rightarrow$ 3d) edges, separated by ~17 eV, which reflects the spin–orbit splitting of the Ni 2p level. The intensity ratio I_{L3}/I_{L2} provides insight into the oxidation state: in metallic Ni, the L_3 peak is only moderately stronger, whereas in NiO the L_3 peak becomes significantly enhanced due to a higher number of unoccupied 3d states. The measured spectrum, with the L_3 edge at 852 eV and the L_2 edge at 869 eV, indicates a slight chemical shift to higher energies, consistent with the presence of oxidized Ni species probably due to residual nickel in the nickel-depleted Mg(Ni)O support and/or as a result of passivation. Notably, after 100 h on stream the overall intensity of the Ni-L signals decreased significantly, suggesting a reduction of the detectable Ni contribution, most likely due to progressive oxidation or structural modification during operation. Same was observed for Mg (Figure S11).

View Article Online
DOI: 10.1039/D6CY00548A

By comparing the morphology of the preformed with the post-reaction catalyst after 100 h TOS using HR-TEM (Figure 11), TEM-EDX (Figure 12) and SEM-EDX (Figure S10) distinct changes that have occurred under reaction conditions are observable. After the preforming, the NM5050 catalyst shows crystallite sizes are around 5 nm in diameter with random orientations as indicated by the lattice fringes. This is in good agreement with the PXRD (Figure 2) and electron diffraction results (Fig. S8). The particles show sharp edges and are faceted but smooth out during the reaction, creating more roundish crystallites with only slightly increasing diameters. It, however, remains unclear to what extent these morphological changes are due to the exposure to the reaction feed or the passivation.

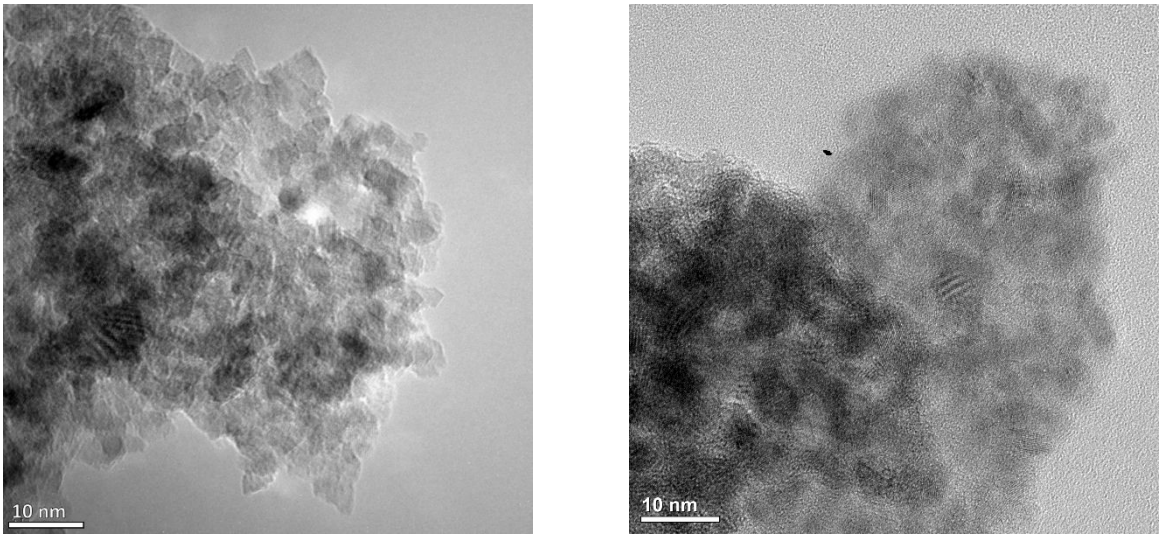

Figure 11: HR-TEM micrographs comparing the NM5050 catalyst after the preforming step (left) and after 100 h time-on-stream (right).

Changes of the NM5050 catalyst in its microstructure and element distribution between the three different stages preformed, post-reaction (3h TOS) and post-reaction (100h TOS) are revealed by TEM-EDX elemental maps (Fig.12). In agreement with the findings of PXRD, the Ni particles are rather small directly after pre-formation, they sinter significantly under reaction conditions in the initial phase after 3h TOS. Despite the longer reaction time and the variations of reaction conditions during the resilience test, they hardly increase further in size up to 100h TOS. Furthermore, no coke formation has been observed from the post-mortem elemental mappings.

View Article Online
DOI: 10.1039/D6CY00548A

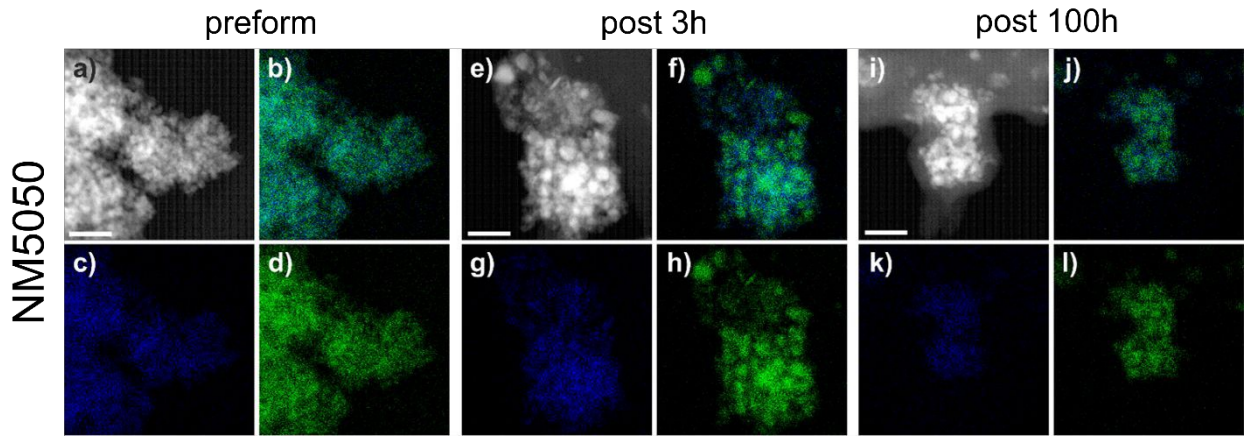

Figure 12: EDX elemental mappings each showing ADF-STEM image (a), e), i)) overlay (b), f), j)) of the Mg (c), g), k)) and the Ni maps (d), h), l)). (a-d) NM5050 preform, (e-h) NM5050 post-reaction 3 h, (i-l) NM5050 post-reaction 100 h. The scale bar represents 30 nm in all cases.

View Article Online
DOI: 10.1039/D6CY00548A

Conclusion

In this work, the performance of recently developed nanoscale nickel-magnesium oxide (NM) catalysts derived from a coprecipitated bimetallic single source precursor was compared to a commercial Ni/Al_2O_3 catalyst and an impregnated benchmark Ni/MgO catalyst both under steady-state and fluctuating methanation conditions for 100 h time-on-stream in a fixed-bed reactor. Moreover, changes in morphology, microstructure and phase composition after reaction have been investigated using PXRD, HR-TEM and EELS.

All NM catalysts show high initial CO_2 conversion >80% at 10 bar and 300 °C under steady-state conditions with high methane selectivities >98% outperforming both the commercial Ni/Al_2O_3 and the Ni/MgO catalyst. The high specific surface area of the fresh starting material decreases due to reductive preforming while a higher magnesium fraction helps to keep the formed nickel particles in a small size. By adjusting the methanation temperature, a maximum conversion of 89% was found for the NM5050 catalyst at 260 °C and 10 bar, which is the catalyst with the highest magnesium content and smallest nickel particles. With an increased pressure of 20 bar, the CO_2 conversion could be increased up to 92%. The same trend was observed for the other NM catalysts, but with a shift to higher temperatures, slightly lower conversion, and minor changes in selectivity.

Furthermore, the best performing NM 5050 catalyst was benchmarked to a commercial Ni/Al_2O_3 catalyst over a period of 100 h time-on-stream (TOS) under fluctuating conditions to test the catalysts resilience and stability under dynamic reaction conditions simulating a potential realistic operating environment. The NM5050 showed a high resilience against all changes. CO_2 conversion of 30% and CH_4 selectivity of up to 70% are still achievable with a deficient 1/1 CO_2/H_2 gas phase ratio, while for the Ni/Al_2O_3 the performance dropped to 20% conversion and only 50% CH_4 selectivity. This shows that the competing RWGS is more suppressed, favoring the NM5050 over the Ni/Al_2O_3 catalyst for use cases with varying hydrogen inflow. Furthermore, higher space velocities lead to higher CO_2 conversion and an overall higher CH_4 productivity. No deactivation at temperatures up to 400 °C was observed for both catalysts as well, suggesting a resilience against potential hot spots or sintering. Based on the powder XRD and electron microscopy studies of the spent NM5050, it can be concluded that the crystallite growth is minimal, even under fluctuating reaction conditions.

View Article Online
DOI: 10.1039/D6CY00548A

Further optimizing the reaction conditions, reducing the amount of purge gas being used, and by removing the excess nitrogen via a membrane could result in a gas composition that meets the requirements for entry into the general gas grid. A lower optimal operation temperature of 260 °C (compared to traditional methanation) is favorable when combining it with the use of waste heat and CO_2 often generated in industrial processes or decentralized combined heat and power plants. With hydrogen generated from excess renewable energy, this could solve the challenge of long-term hydrogen storage and help us move towards a circular carbon economy.

Acknowledgements

The authors kindly acknowledge funding by the DFG via the SPP2080 project (grant no. 406903668) and the financial support by the state of Schleswig-Holstein. We kindly acknowledge the central analytics department and the X-Ray Service Facility at the University of Hamburg for ICP-OES measurements. In addition, the authors acknowledge Prof. Lorenz Kienle and the TEM center of Kiel University for the TEM and EDX measurements. Open Access funding enabled and organized by Project DEAL.

Conflict of Interests

There are no conflicts to declare.

Data Availability Statement

The data that support the findings of this study are available from the corresponding author upon reasonable request.

View Article Online
DOI: 10.1039/D6CY00548A

References

[1] I. P. o. C. Change, Climate Change 2022 - Mitigation of Climate Change, Cambridge University Press **2023**.

[2] L. Jing, H. M. El-Houjeiri, J.-C. Monfort, A. R. Brandt, M. S. Masnadi, D. Gordon, J. A. Bergerson, Nat. Clim. Chang. **2020**, 10 (6), 526–532. DOI: 10.1038/s41558-020-0775-3.

[3] J. Li, P. Tharakan, D. Macdonald, X. Liang, Energy Policy **2013**, 61, 1377–1387. DOI: 10.1016/j.enpol.2013.05.082.

[4] K. de Ras, R. van de Vijver, V. V. Galvita, G. B. Marin, K. M. van Geem, Current Opinion in Chemical Engineering **2019**, 26, 81–87. DOI: 10.1016/j.coche.2019.09.001.

[5] A. Arasto, E. Tsupari, J. Kärki, M. Sihvonen, J. Lilja, Energy Procedia **2013**, 37, 7117–7124. DOI: 10.1016/j.egypro.2013.06.648.

[6] M. Xu, A. R. Jupp, M. S. E. Ong, K. I. Burton, S. S. Chitnis, D. W. Stephan, Angewandte Chemie **2019**, 131 (17), 5763–5767. DOI: 10.1002/ange.201900058.

[7] J. Ding, R. Ye, Y. Fu, Y. He, Y. Wu, Y. Zhang, Q. Zhong, H. H. Kung, M. Fan, Nature communications **2023**, 14 (1), 4586. DOI: 10.1038/s41467-023-40351-5.

[8] T. Iijima, T. Yamaguchi, Applied Catalysis A: General **2008**, 345 (1), 12–17. DOI: 10.1016/j.apcata.2008.03.037.

[9] C. J. Whiteoak, N. Kielland, V. Laserna, E. C. Escudero-Adán, E. Martin, A. W. Kleij, Journal of the American Chemical Society **2013**, 135 (4), 1228–1231. DOI: 10.1021/ja311053h.

[10] J. Mahabir, K. Bhagaloo, N. Koylass, M. N. Boodoo, R. Ali, M. Guo, K. Ward, Journal of CO2 Utilization **2021**, 45, 101451. DOI: 10.1016/j.jcou.2021.101451.

[11] P. Schühle, R. Stöber, M. Gierse, A. Schaadt, R. Szolak, S. Thill, M. Alders, C. Hebling, P. Wasserscheid, O. Salem, Energy Environ. Sci. **2023**, 16 (7), 3002–3013. DOI: 10.1039/D3EE00228D.

[12] J. Albert, A. Jess, C. Kern, F. Pöhlmann, K. Glowienka, P. Wasserscheid, ACS Sustainable Chem. Eng. **2016**, 4 (9), 5078–5086. DOI: 10.1021/acssuschemeng.6b01531.

[13] J. Wang, S. Chen, P. Ticali, P. Summa, S. Mai, K. Skorupska, M. Behrens, Nanoscale **2024**, 16 (37), 17378–17392. DOI: 10.1039/D4NR02025A.

[14] IEA, Gas Market Report Q2-2023 **2023**.

View Article Online
DOI: 10.1039/D6CY00548A

[15] C. Dannesboe, J. B. Hansen, I. Johannsen, React. Chem. Eng. **2020**, 5 (1), 183–189. DOI: 10.1039/C9RE00351G.

[16] J. Kopyscinski, T. J. Schildhauer, S. M. Biollaz, Fuel **2010**, 89 (8), 1763–1783. DOI: 10.1016/j.fuel.2010.01.027.

[17] L. Shen, J. Xu, M. Zhu, Y.-F. Han, ACS Catal. **2020**, 10 (24), 14581–14591. DOI: 10.1021/acscatal.0c03471.

[18] J. Huang, X. Li, X. Wang, X. Fang, H. Wang, X. Xu, Journal of CO2 Utilization **2019**, 33, 55–63. DOI: 10.1016/j.jcou.2019.04.022.

[19] S. Chen, Y. H. Hu, Surface Innovations **2025**, 13 (2), 84–94. DOI: 10.1680/jsuin.24.00103.

[20] C. Cerdá-Moreno, A. Chica, S. Keller, C. Rautenberg, U. Bentrup, Applied Catalysis B: Environmental **2020**, 264, 118546. DOI: 10.1016/j.apcatb.2019.118546.

[21] B. Mutz, H. W. P. Carvalho, W. Kleist, J.-D. Grunwaldt, J. Phys.: Conf. Ser. **2016**, 712, 12050. DOI: 10.1088/1742-6596/712/1/012050.

[22] B. Kreitz, J. Friedland, R. Güttel, G. D. Wehinger, T. Turek, Chemie Ingenieur Technik **2019**, 91 (5), 576–582. DOI: 10.1002/cite.201800191.

[23] T. Stiegler, K. Meltzer, A. Tremel, M. Baldauf, P. Wasserscheid, J. Albert, Energy Technology **2019**, 7 (6), 1900047. DOI: 10.1002/ente.201900047.

[24] K. F. Kalz, R. Kraehnert, M. Dvoyashkin, R. Dittmeyer, R. Gläser, U. Krewer, K. Reuter, J.-D. Grunwaldt, ChemCatChem **2017**, 9 (1), 17–29. DOI: 10.1002/cctc.201600996.

[25] P. Kampe, N. Herrmann, C. Ruhmlieb, M. Finsel, O. Korup, R. Horn, J. Albert, ACS Sustainable Chem. Eng. **2024**, 12 (25), 9541–9549. DOI: 10.1021/acssuschemeng.4c03279.

[26] A. A. Coelho, J Appl Crystallogr **2018**, 51 (1), 210–218. DOI: 10.1107/S1600576718000183.

[27] R. W. Cheary, A. A. Coelho, J. P. Cline, Journal of research of the National Institute of Standards and Technology **2004**, 109 (1), 1–25. DOI: 10.6028/jres.109.002.

[28] D. Balzar, N. Audebrand, M. R. Daymond, A. Fitch, A. Hewat, J. I. Langford, A. Le Bail, D. Louër, O. Masson, C. N. McCowan, N. C. Popa, P. W. Stephens, B. H. Toby, J Appl Crystallogr **2004**, 37 (6), 911–924. DOI: 10.1107/S0021889804022551.

[29] A. Wolf, M. Chumakovski, H. Rohr, P. Hauberg, M. Saedi, S. Mangelsen, M. Behrens, ChemSusChem **2025**, 18 (23), e202502052. DOI: 10.1002/cssc.202502052.

[30] J. Gao, Q. Liu, F. Gu, B. Liu, Z. Zhong, F. Su, RSC Adv. **2015**, 5 (29), 22759–22776. DOI: 10.1039/C4RA16114A.

View Article Online
DOI: 10.1039/D6CY00548A

[31] K. Wang, X. He, X. Liang, International Journal of Hydrogen Energy **2024**, 66, 195–207. DOI: 10.1016/j.ijhydene.2024.04.060.

[32] N. Takezawa, H. Terunuma, M. Shimokawabe, H. Kobayashib, Applied Catalysis **1986**, 23 (2), 291–298. DOI: 10.1016/S0166-9834(00)81299-3.

[33] M. Guo, G. Lu, Catalysis Communications **2014**, 54, 55–60. DOI: 10.1016/j.catcom.2014.05.022.

[34] Y. Ma, J. Liu, M. Chu, J. Yue, Y. Cui, G. Xu, Catal Lett **2020**, 150 (5), 1418–1426. DOI: 10.1007/s10562-019-03033-w.

[35] X. Jia, X. Zhang, N. Rui, X. Hu, C. Liu, Applied Catalysis B: Environmental **2019**, 244, 159–169. DOI: 10.1016/j.apcatb.2018.11.024.

[36] S. Tada, T. Shimizu, H. Kameyama, T. Haneda, R. Kikuchi, International Journal of Hydrogen Energy **2012**, 37 (7), 5527–5531. DOI: 10.1016/j.ijhydene.2011.12.122.

[37] S. Abate, C. Mebrahtu, E. Giglio, F. Deorsola, S. Bensaid, S. Perathoner, R. Pirone, G. Centi, Ind. Eng. Chem. Res. **2016**, 55 (16), 4451–4460. DOI: 10.1021/acs.iecr.6b00134.

[38] Y. Shimomura, Z. Nishiyama, Mem. Inst. Sci. Ind. Res. Osaka Univ. **1948**, 6, 30, University.

[39] W. L. BRAGG, Nature **1920**, 105 (2647), 646–648. DOI: 10.1038/105646a0.

[40] Y. H. Hu, Catalysis Today **2009**, 148 (3-4), 206–211. DOI: 10.1016/j.cattod.2009.07.076.

[41] Y. H. Hu, E. Ruckenstein, Journal of Catalysis **1996**, 163 (2), 306–311. DOI: 10.1006/jcat.1996.0331.

[42] K. Ghaib, K. Nitz, F.-Z. Ben-Fares, ChemBioEng Reviews **2016**, 3 (6), 266–275. DOI: 10.1002/cben.201600022.

[43] S. Park, K. Choi, C. Lee, S. Kim, Y. Yoo, D. Chang, International Journal of Hydrogen Energy **2021**, 46 (41), 21303–21317. DOI: 10.1016/j.ijhydene.2021.04.015.

[44] Z. Lv, H. Du, S. Xu, T. Deng, J. Ruan, C. Qin, Applied Energy **2024**, 355, 122242. DOI: 10.1016/j.apenergy.2023.122242.

[45] H.E. Swanson, E.Tatge, Circular, Vol. 539, National Bureau of Standards, **1953**, 1–95.

Data Availability

View Article Online
DOI: 10.1039/D6CY00548A

The data that support the findings of this study are available from the corresponding author upon reasonable request.